Le Corvec, N., Walter, T. R., Ruch, J., Bonforte, A., Puglisi, G. (2014): Experimental study of the interplay between magmatic rift intrusion and flank instability with application to the 2001 Mount Etna eruption. - *Journal of Geophysical Research*, *119*, 7, p. 5356-5368

DOI: http://doi.org/10.1002/2014JB011224

AGU PUBLICATIONS

JGR

Journal of Geophysical Research: Solid Earth

RESEARCH ARTICLE
10.1002/2014JB011224

Special Section:
Stress, Strain and Mass Changes at Volcanoes

Key Points:
- Analyzing Mount Etna east flank dynamics during the 2001 eruption
- Good correlation between analogue models and GPS data
- Understanding the different behavior of faulting before/during/after an eruption

Correspondence to:
N. Le Corvec,
lecorvec@lpi.usra.edu

Citation:
Le Corvec, N., T. R. Walter, J. Ruch, A. Bonforte, and G. Puglisi (2014), Experimental study of the interplay between magmatic rift intrusion and flank instability with application to the 2001 Mount Etna eruption, *J. Geophys. Res. Solid Earth*, *119*, 5356–5368, doi:10.1002/2014JB011224.

Received 24 APR 2014
Accepted 10 JUN 2014
Accepted article online 16 JUN 2014
Published online 10 JUL 2014

# Experimental study of the interplay between magmatic rift intrusion and flank instability with application to the 2001 Mount Etna eruption

**Nicolas Le Corvec[1], Thomas R. Walter[2], Joel Ruch[3], Alessandro Bonforte[4], and Giuseppe Puglisi[4]**

[1]Lunar and Planetary Institute, USRA, Houston, Texas, USA, [2]GFZ German Research Centre for Geosciences, Potsdam, Germany, [3]King Abdullah University of Science and Technology, Thuwal, Saudi Arabia, [4]Istituto Nazionale di Geofisica e Vulcanologia – Sezione di Catania, Osservatorio Etneo, Catania, Italy

**Abstract** Mount Etna volcano is subject to transient magmatic intrusions and flank movement. The east flank of the edifice, in particular, is moving eastward and is dissected by the Timpe Fault System. The relationship of this eastward motion with intrusions and tectonic fault motion, however, remains poorly constrained. Here we explore this relationship by using analogue experiments that are designed to simulate magmatic rift intrusion, flank movement, and fault activity before, during, and after a magmatic intrusion episode. Using particle image velocimetry allows for a precise temporal and spatial analysis of the development and activity of fault systems. The results show that the occurrence of rift intrusion episodes has a direct effect on fault activity. In such a situation, fault activity may occur or may be hindered, depending on the interplay of fault displacement and flank acceleration in response to dike intrusion. Our results demonstrate that a complex interplay may exist between an active tectonic fault system and magmatically induced flank instability. Episodes of magmatic intrusion change the intensity pattern of horizontal flank displacements and may hinder or activate associated faults. We further compare our results with the GPS data of the Mount Etna 2001 eruption and intrusion. We find that syneruptive displacement rates at the Timpe Fault System have differed from the preeruptive or posteruptive periods, which shows a good agreement of both the experimental and the GPS data. Therefore, understanding the flank instability and flank stability at Mount Etna requires consideration of both tectonic and magmatic forcing.

## 1. Introduction

Basaltic volcanoes are prone to complex deformation processes related to magmatic intrusions, gravitational loading, and tectonic activity. These processes are observed especially at large volcanoes (e.g., Mounts Etna and Kilauea) and are thought to be related to various forms of flank instabilities [*Siebert*, 1992; *Walter and Troll*, 2003]. Mount Etna (Figure 1) is one of the largest and most active continental basaltic volcanoes on Earth, characterized by a complex deformation pattern, related with fault activity. This includes periods of uplift and subsidence related to magma movement at depth, a continuous motion of large sectors of its east flank and episodes of dike intrusions occurring mainly along two of the three rift zones [*McGuire*, 1989; *Borgia et al.*, 1992; *Rasa et al.*, 1996; *Monaco et al.*, 1997; *Froger et al.*, 2001; *Solaro et al.*, 2010].

Magmatic rift intrusions and flank instability at Mount Etna are thought to be interacting, because dike intrusions accelerate movement of the flank, which in turn affects the dynamics and geometry of dike intrusions [*McGuire and Pullen*, 1989; *Borgia et al.*, 1992; *Le Corvec and Walter*, 2009]. Because of these complex relations and because of its continuous activity, Mount Etna is an ideal case to analyze the interplay between magmatism and tectonic activity. The motion of the east flank is mainly accommodated by blocks [*Neri et al.*, 2005] dissected by active faulting [*Bonforte et al.*, 2008; *Azzaro et al.*, 2013; *Barreca et al.*, 2013]. Some of the faults have developed in response to local volcano-tectonic activity, such as the Pernicana Fault System (PFS, Figure 1), while others are thought to be more controlled by regional tectonic processes (e.g., the Timpe Fault System (TFS), Figure 1) [*Bonaccorso et al.*, 1996]. The TFS is dissecting the eastern flank of Mount Etna and is oriented in NNW-SSE direction, and may even be linked to the much larger Malta Escarpment as some early work suggests [*Kieffer*, 1985; *Monaco and Tortorici*, 2000]. Although recent studies question a direct connection of the TFS and the Malta escarpment being the faults themselves

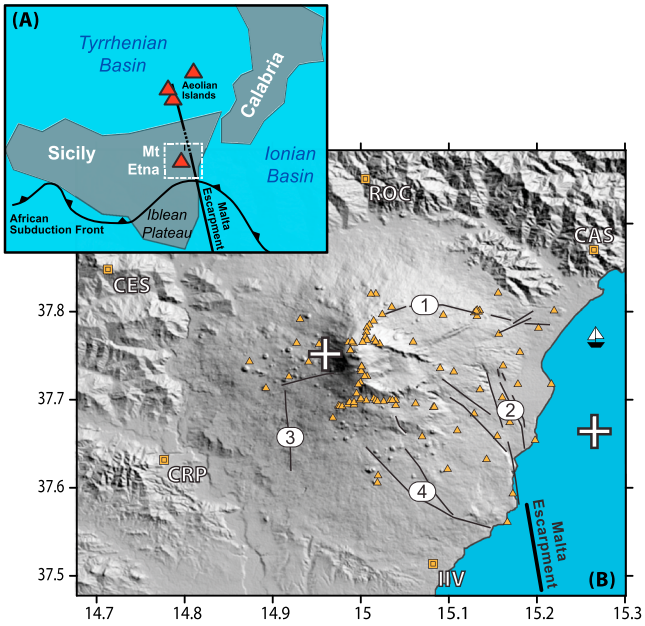


**Figure 1.** (a) Location of Mount Etna and other active volcanoes (shown by red triangles) on Sicily and sketch of the inferred Malta escarpment. (b) Shaded relief map showing Mount Etna volcano and the major active faults. The triangle-shaped symbols represent the campaign GPS network; the square-shaped symbols represent permanent GPS stations as of 2001. Numbers denote the Pernicana fault system (1), the Timpe Fault System (2), the Ragalna Fault System (3), and the Tremestieri-Trecastagni Fault System (4). The two white crosses indicate the extent of the cross section in Figure 3.

involved in the seaward motion of the eastern flank [*Bonforte and Puglisi*, 2006], the TFS is identified as a crustal scale feature with an origin different than from gravitational sliding [*Argnani et al*., 2013]. Our testable question then was, how is the interplay between flank acceleration, gravitational sliding, and the movement along the crustal scale TFS that is dissecting the east flank of Mount Etna?

The interplay between faulting and magmatic intrusion at Etna is well known; however, the particular way how flank motion and displacement of crustal faults interfere remains to be studied. To better understand this relationship, we use analogue models to simulate and test the effect of regional tectonics on dike intrusion and flank motion, and conversely. We further compare our experimental results with GPS data collected and analyzed during the 2001 eruption.

## 2. Background

### 2.1. Structural Setting of Mount Etna

Mount Etna is a polygenic volcano located in the eastern part of Sicily (Figure 1). Its structural evolution is linked with the regional tectonic setting, being located at the intersection of a zone of N-S shortening due to the collision between the African and European plates, and a zone of WNW-ESE extension associated with the rollback of the Ionian microplate [*Lentini*, 1982]. A complex deformation pattern characterizes the entire east and south flanks of the volcano. The unstable volcano east flank is bounded by the Pernicana Fault System (PFS; Figure 1) to the north [*Acocella and Neri*, 2005; *Ruch et al*., 2013], and to the south the sliding is progressively reduced by several faults [*Azzaro et al*., 2013] and mainly enclosed by the Trecastagni fault [*Bonforte et al*., 2013b]. A minor southward spreading still affects also the southern flank of the volcano and the sliding motion is completely closed on the southwestern side by the Ragalna fault [*Rust and Neri*, 1996]. The eastward motion is apparently accommodated at depth by a décollement, which the geometric and kinematic details are still a matter of debate. One inferred depth of the décollement is around 4 km below sea level [e.g., *Bousquet and Lanzafame*, 2001; *Puglisi and Bonforte*, 2004; *Ruch et al*., 2010]. Several studies propose a feedback process between intrusions along rift zones, transient slip acceleration along the PFS, and motion along the décollement [*Walter et al*., 2005; *Currenti et al*., 2008; *Alparone et al*., 2013].

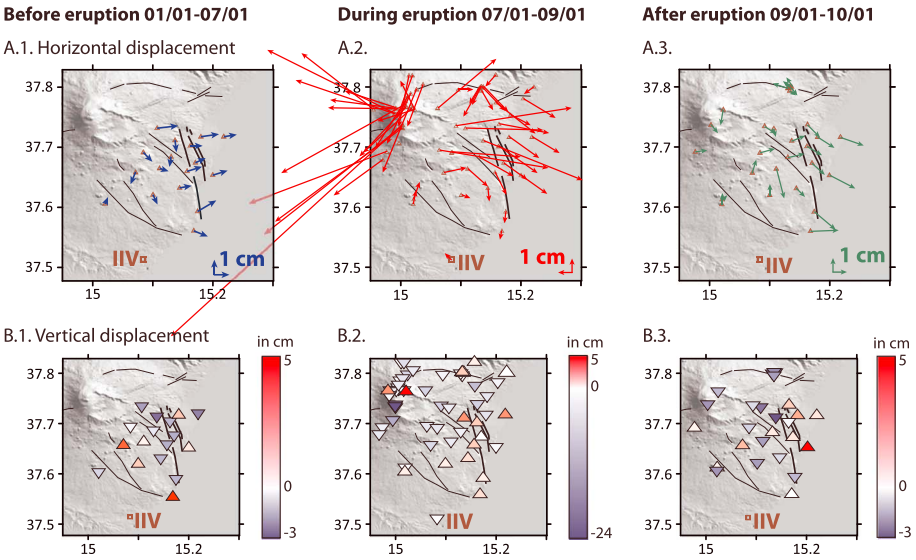


**Figure 2.** GPS data illustrating the 2001 episode on Mount Etna [after *Puglisi et al.*, 2008]. Columns show the dynamics of Mount Etna before, during, and after the July–August 2001 eruption. The horizontal displacement (a1) before, (a2) during, and (a3) after the eruption. The vertical displacement (b1) before, (b2) during, and (b3) after the eruption. The GPS data illustrates that without rifting intrusions, the largest horizontal and vertical displacements occur close to the coast, east of the Timpe Fault System. During eruption, displacements are largest close to the rift, while normal faulting at the Timpe Fault System appears inactive. Black lines represent the major faults affecting Mount Etna. Reference vector scale = 1 cm displacement, color scale bar in Figures 2b1–2b3 is displacement in cm showing uplift (red) and subsidence (blue). The black lines represent the regional fault system; the thick black lines represent the Timpe Fault System.

The east flank is also affected by the TFS [*Azzaro*, 1999], which is considered by several authors as the surface expression of the regional Malta escarpment separating the continental Iblean Plateau from the oceanic Ionian Basin [*Lentini*, 1982; *Bonaccorso*, 1996] (Figure 1). GPS data demonstrated that TFS is involved in the eastward motion of the volcano flank [*Bonforte and Puglisi*, 2006]. Some recent studies integrating marine and onshore structural data propose to reinterpret TFS as part of an instable system affecting the volcano together with the entire the continental margin [*Chiocci et al.*, 2011]. Others interpret the TFS as a crustal structure and not a shallow fault system related to Mount Etna gravitational sliding [*Argnani et al.*, 2013].

Ground deformation at Mount Etna has been continuously monitored over three decades using leveling, electronic distance measurement (EDM), GPS, and interferometric synthetic aperture radar (InSAR) data [*Bonforte and Puglisi*, 2006; *Houlie et al.*, 2006; *Solaro et al.*, 2010]. These deformation patterns enable detailed observations on the flank kinematics and magmatic processes involved before, during, and after eruptions. A few examples are the following: (i) leveling and EDM networks evidenced the eastward directed block movements due to dike intrusion [e.g., *McGuire et al.*, 1990], (ii) tilt data contributed to measure dike propagation [*Bonaccorso and Davis*, 1993], (iii) GPS campaigns started in 1988 [*Briole et al.*, 1992] and together with permanent GPS stations are still one of the main system used to study ground deformation at Mount Etna [e.g., *Bonforte et al.*, 2008; *Puglisi et al.*, 2008], and (iv) InSAR has been used to measure ground deformation for specific intrusive periods [*Froger et al.*, 2001; *Lundgren et al.*, 2004; *Puglisi et al.*, 2008; *Bonforte et al.*, 2011], or over longer periods using time series analysis [*Ruch et al.*, 2010; *Solaro et al.*, 2010]. In the following we detail the 2001 eruption that we further used as an example to compare the analogue experimental results with a natural case.

### 2.2. The 2001 Eruption

The 2001 eruption was one of the largest flank eruptions on Mount Etna since 1993 [*Behncke and Neri*, 2003]. The eruption started on 17 July 2001 accompanied by thousands of low-magnitude earthquakes, located at about 3 km below sea level, interpreted as an upward migration of magma [*Patane et al.*, 2003]. The eruption started at the summit of the volcano, followed by an eccentric eruption along the southern rift zone [*Behncke and Neri*, 2003]. Analytical models based on GPS and seismic data suggest that the 2001 event was generated by a 3 m thick dike oriented in N-S direction [*Bonaccorso et al.*, 2002; *Patane et al.*, 2002]. When reaching the surface, the dike produced a series of eruptive fissures mainly oriented N-S from 2570 m down to 2100 m above

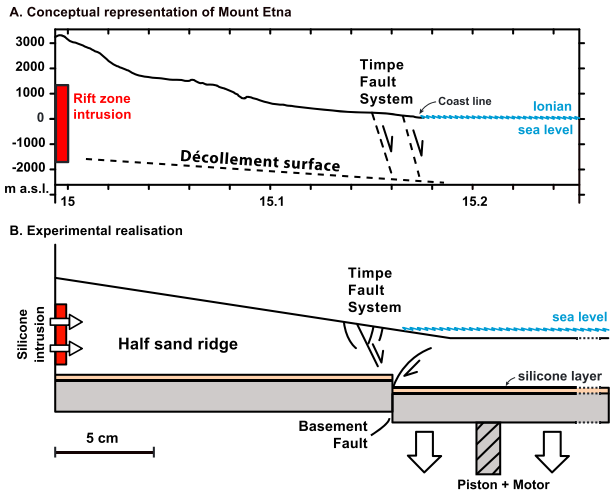


**Figure 3.** Cross section of the east flank. (a) Conceptual representation of the location of the Timpe Fault System, the décollement surface, and the active rift zone. (b) Experimental realization of the Mount Etna's structural configuration. Experiments were designed in a sandbox, limited by two panes of glass at the back and front of the model. This defined a sand wedge, simulating the east flank of Mount Etna. A silicone intrusion occurred from the left to simulate rifting and was controlled by the opening or closing of the tank trapdoor on the left side. A décollement surface was defined by viscous silicone, too. A crustal fault approximately beneath the location of the Timpe fault was simulated by a motor-controlled piston subsiding on the eastern half of the setup. The crustal fault divides the model into a stable part on its left (17 cm) and a subsiding part on its right (63 cm). The experiments were recorded in side view by a CCD camera using digital cross-correlation technique, allowing detection of submillimeter displacements to analyze the deformation in time.

sea level, characterized by Hawaiian and Strombolian activities producing lava flows propagating southward [*Behncke and Neri*, 2003]. The effusive activity decreased until 9 August, marking the end of the eruption.

Ground deformation patterns show that the intrusion mostly affected the volcano east flank [*Puglisi et al.*, 2008]. Prior to the eruption, the east flank was moving eastward at a rate of around 1 cm/yr (Figure 2a1) [*Solaro et al.*, 2010]. The GPS data show acceleration of the east flank of up to ~10 cm/yr and subsidence of the lower flank of the volcano (Figures 2a2 and 2b2) [*Puglisi et al.*, 2008]. The flank acceleration was first revealed by geodetic and seismic data during the last hours of the intrusion process. The deformation field propagated from the upper part of the volcano to the shoreline and was detected by geodetic surveys carried out during the eruption [*Bonforte et al.*, 2004]. Following the eruption, the deformation affecting the volcano upper part ceased, while displacement along the shoreline (i.e., to the east of the TFS) increased, there reaching localized uplift of a few centimeters (Figures 2a3 and 2b3) together with seismicity [*Puglisi et al.*, 2008].

## 3. Experimental Setup and Scaling

### 3.1. Setup

The experimental setup consists of a sandbox (80 × 20 × 10 cm) made of glass panes in order to allow image recording from the sides using cameras. To simulate Mount Etna unstable east flank, we approximate the topography with a half sand ridge (45 cm length, 8 cm high, and 10 cm deep, Figure 3b). The half ridge is placed on top of a silicone layer representing a basal décollement. The half sand ridge is buttressed on its left side by a tank filled with silicone. The tank possesses a trapdoor that can be lifted up and down at a chosen height allowing its opening or closure. Opening of the trapdoor simulates the intrusion of silicone within the sand ridge, as a dike would intrude one of the rift zones of Mount Etna. The upper and the lower limits of the silicone intrusions are controlled during the experiment and systematically varied in different experiments. Also, the thickness of the intrusions was controlled; the experiments were stopped after simulation of 1 cm thick intrusion. The general experimental setup and the simulation of magmatic rift intrusion into a volcanic edifice are similar to that described in *Le Corvec and Walter* [2009].

In these Mount Etna-related experiments, the right side of the model remains unbuttressed, but it is subjected to additional complexity (Figure 3b). To simulate the TFS activity (i.e., crustal tectonic), the sandbox

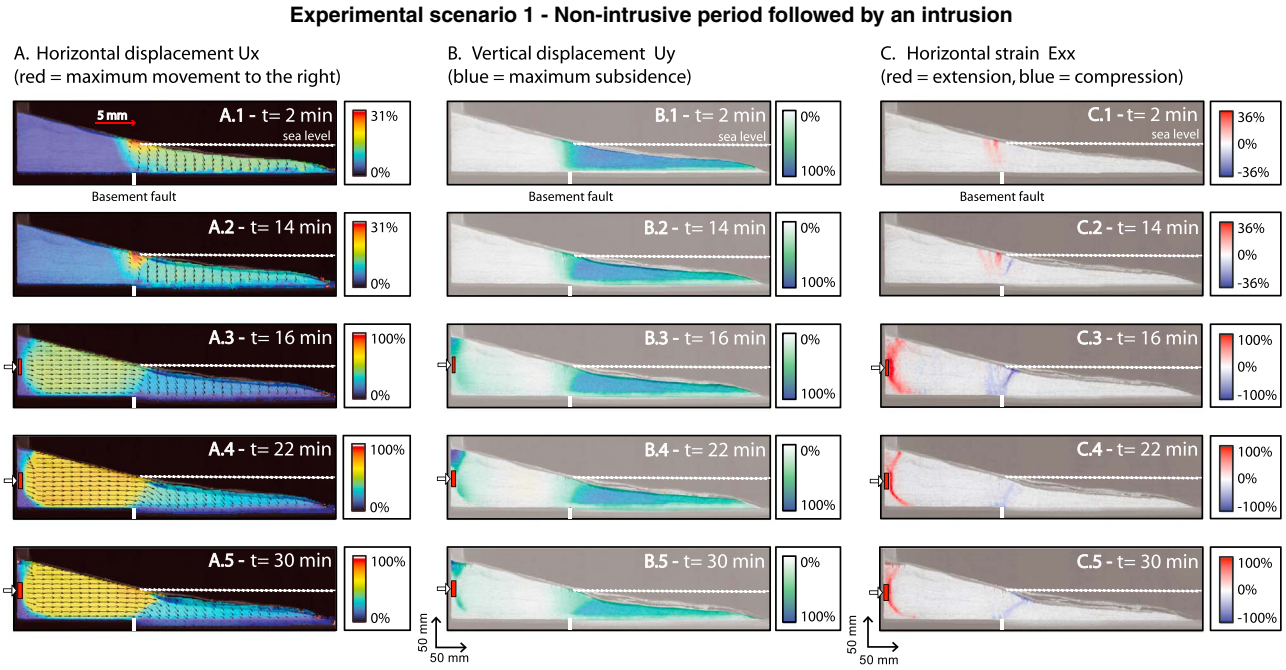


**Figure 4.** Results of the experimental scenario where a nonintrusive period was simulated and followed by an intrusion simulation. Displacement of the sand ridge was first affected by (a1, b1, c1, a2, b2, and c2) the downward displacement of the moving block creating normal faults. The rest of the ridge stays stable. Once the intrusion is initiated, the stable part of the wedge is affected by (a3, b3, and c3) horizontal displacement to the right. The normal faults (red in Figures 4c1 and 4c2) are clamped, whereas thrust faulting dominates (blue in Figures 4c3–4c5). With continuous rifting, also the dip of the thrust faults above the crustal fault becomes shallower. The rows show images taken at 2, 14, 16, 22, and 30 min into the experiment. Figures 4a1–4a5 show the horizontal displacements (Ux), Figures 4b1–4b5 show the vertical displacement (Uy), and Figures 4c1–4c5 show the horizontal strain (Exx). Color scales are indicated, the reference vector of 5 mm is shown in Figure 4a1. See Figure 6a for the structural summary of the active and inactive faults.

base consisted of a stable part (17 cm in length) and a subsiding part (63 cm in length), the latter moving downward (normal fault kinematics) using a piston, activated by a motor (Figure 3b). The velocity of the piston is regulated to a constant rate of 2 cm/h (0.0006 m/s).

Therefore, the experiments consist of a volcanic flank (half sand ridge), a basal décollement (silicone layer), and a constantly moving crustal fault dissecting the lower flank (simulating the TFS). All we vary is the influence of intrusive push within the volcanic flank.

### 3.2. Scaling

To respect similarities to nature, models have to be geometrically, kinematically, and dynamically scaled [*Hubbert*, 1937; *Ramberg*, 1981]. The geometry of the model was scaled in order to have the boundary between the stable and unstable part of the base at the location of the TFS in nature. We chose a length ratio $L^*$ between model and nature of $10^{-5}$ (1 cm of the model corresponding to ~1 km in nature). The sand ridge was made of a mixture of ~1600 kg m$^{-3}$ of sand and 13% starch (cohesive material) to reproduce natural volcanic rock behavior (volcanic rocks ~ 2600 kg m$^{-3}$) [*Burchardt and Walter*, 2010]. The density ratio between the analogue materials and the natural rocks is $\rho^* \sim 0.6$. The gravitational acceleration is identical in nature and in our models, with $g^* = 1$. Therefore, the stress ratio $\sigma^*$ between our models and nature can be calculated as follows:

$$\sigma^* = \rho^* g^* L^*$$

The stress ratio is $\sigma^* = 6 \times 10^{-6}$. Therefore, our models are about $6 \times 10^6$ times weaker than natural volcanic systems. Mohr-Coulomb failure criterion is assumed for the volcanic edifice.

The cohesion and angle of friction in our model must therefore be similar to nature. The cohesion of volcanic rocks ranges from between $10^6$ and $10^8$ Pa, and their angle of internal friction is around 30°–35° [*Schellart*, 2000]. The corresponding cohesion of our analogue material must be around 10° and $10^2$ Pa, which is compatible with the cohesion of our sand and starch mixture (~70 Pa [*Burchardt and Walter*, 2010]). The angle of friction of the mixture is ~28° [*Burchardt and Walter*, 2010].

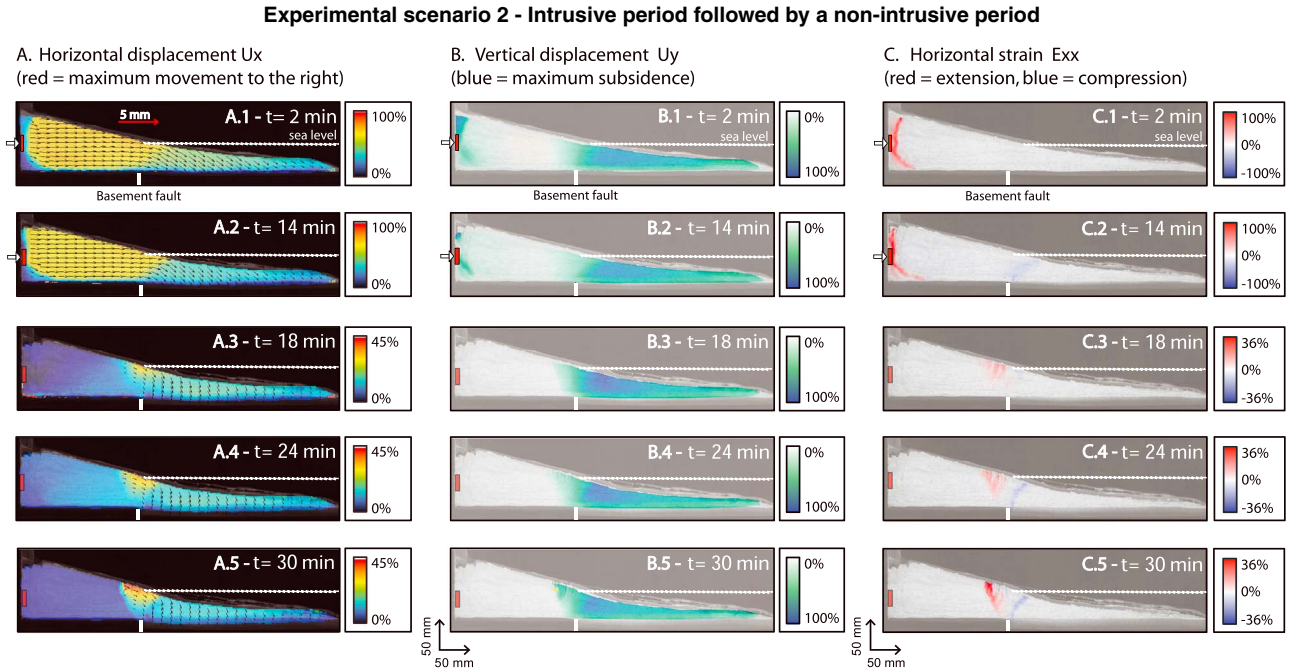


**Figure 5.** Results of the experimental scenario where an intrusive period was simulated, and where then the intrusion ceased. (a1 and a2) The left part of the sand ridge is first affected by horizontal displacement as the silicone intrudes; (b1 and b2) the right part is subsiding above the downward moving plate. When the intrusion is stopped, the left part of the sand ridge becomes stable while the right part is still affected by (b3–b5) vertical displacement (c3–c5) forming and reactivating normal faults. The rows show images taken at 2, 14, 18, 24, and 30 min into the experiment. Figures 5a1–5a5 show horizontal displacements (Ux), Figures 5b1–5b5 show the vertical displacement (Uy), and Figures 5c1–5c5 show the horizontal strain (Exx). Color scales are indicated, the reference vector of 5 mm is shown in Figure 5a1. See Figure 6b for the structural summary of the active and inactive faults.

In nature, the basal décollement surface (likely made of clay and soft sediments) and the magmatic intrusions are ductile materials. The décollement surface in our experiments is simulated by a silicone layer (~0.4 cm thick with a density of ~1300 kg $m^{-3}$, Figure 3b). Therefore, time ($t$), viscosity ($\mu$), and stress ($\sigma$) must be scaled as follows [*Donnadieu and Merle*, 1998]:

$$\mu^* = \sigma^* t^*$$

The viscosity of clay that composed the Etna volcano base is considered to range from $7.1 \times 10^{14}$ Pa s to $1.3 \times 10^{15}$ Pa s [*Palano et al.*, 2009]. Silicone has a viscosity of ~$10^5$ Pa s, which gives a viscosity ratio for the décollement $\mu_D^*$ ranging from ~$10^{-9}$ to ~$10^{-10}$. The viscosity ratio of the magmatic intrusion ($\mu_M^*$) must therefore equal $\mu_D^*$. The typical viscosity of a basaltic magma is taken as ~$10^4$ Pa s [*Norini and Acocella*, 2011]. The material to be used as an analogue to a basaltic magma in our experiments should therefore have a viscosity ranging from ~$10^{-6}$ to ~$10^{-7}$ Pa s. By using silicone in our experiments, the viscosity difference does not allow the proper scaling of our models. The silicone intrusion is thus representing a relatively high viscous indenter rather than a soft magma body, which allows us to better control the model initialization.

Although our experiments are only approximately scaled, results are mainly qualitative or semiquantitative. We thus show our time-dependent strain rate studies in normalized plots (Figures 4 and 5) and focus the study on the well-scaled development of brittle fractures and their interplay, following the suggestion made by earlier authors [*Merle and Borgia*, 1996; *Roche et al.*, 2000].

The ratios of loading, i.e., the tectonic rate and magmatic intrusion in our model and in nature were of the same order (Table 1) allowing us to compare the deformation occurring in our models to the deformation affecting the east flank of Mount Etna. We note that we did not attempt to model a constant TFS fault displacement. Instead, the block subsidence was held constant, yet the activation and even the localization of the active branches of the TFS are subject to changes.

An important geometric simplification is the scale of the intrusion. While the length may show a realistic relation to the height of the edifice, the intrusion thickness at the end of an experiment largely exceeds

**Table 1.** Scaling Ratios Used in the Experiments[a]

| | Nature | | Models | |
|---|---|---|---|---|
| | Minimum | Maximum | Minimum | Maximum |
| Intrusion rate (Ri) | $6.2 \times 10^{-3}$ m yr$^{-1}$ | $170 \times 10^{-3}$ m yr$^{-1}$ | $3 \times 10^{-2}$ m h$^{-1}$ | $5 \times 10^{-2}$ m h$^{-1}$ |
| Tectonic rate (Rt) | $1.4 \times 10^{-3}$ m yr$^{-1}$ | $2.7 \times 10^{-3}$ m yr$^{-1}$ | $1 \times 10^{-2}$ m h$^{-1}$ | $2 \times 10^{-2}$ m h$^{-1}$ |
| Ratio Rt/Ri | ~0.22 | ~0.016 | ~0.33 | 0.4 |

[a]Natural intrusion rates were taken from *Marinoni* [2001] and *Puglisi et al.* [2008]. Tectonic rates affecting Mount Etna were taken from *Azzaro et al.* [2000]. The length of the silicone intrusion was measured at the end of each experiment, the tectonic rate or subsidence rate was controlled by a motor.

individual dike intrusions thicknesses known from Mount Etna volcano. Therefore, the experiments may better represent a series of intrusions instead of a single dike.

To analyze the kinematics of the experiments, we used a CCD camera that sampled at a rate of one image every 0.5 s. The particle image velocimetry (PIV) uses a digital image cross-correlation technique, which allows to find the best displacement vector between two successive images, and thus, the vector field of the deformation can be extracted [*LaVision*, 2002; *White et al.*, 2003]. Using the resulting vector field, we derive in our experiments different displacement vectors (horizontal Ux and vertical Uy) and the horizontal strain (Uxx). The PIV technique allows for temporal resolution ranging from $10^{-2}$ to $10^{4}$ s, and a spatial resolution ranging from $10^{-2}$ to $10^{3}$ mm [*Adam et al.*, 2005]. The use of a multipass cross-correlation algorithm in the postprocessing increases significantly the accuracy (0.03 to 0.2 pixel) depending on the subsample size [*LaVision*, 2002]. Given an experiment with ~80 cm width and an optical resolution of 4 megapixels, we estimate the absolute accuracy of the length of displacement vectors to be about 0.05 to 0.1 mm.

## 4. Experiment Results

The experiments aimed to simulate two scenarios: first, the deformation and structural changes associated with the beginning of an intrusion (set 1; Figures 4 and 6a); second, the structural changes associated to the residual stress propagation at the end of an intrusion (set 2; Figures 5 and 6b).

### 4.1. Deformation and Structural Change Before and During an Intrusion

The first set of experiments simulates the distal flank of the volcano initially affected only by the continuous subsidence due to the TFS activity and then affected, in the second part of the experiment, also by an intrusion. During the first half of the experiment (Figure 4), only the vertical displacement related to the normal fault is simulated. We observe on the right part of the sand ridge a subsidence and, locally, a high-velocity horizontal displacement (Ux, Figures 4a1 and 4a2) at the surface. This zone also marks the transition to lower vertical displacement velocity to the left (Uy, Figures 4b1 and 4b2), and it is located approximately above the normal fault. The structural development shows formation of extensional structures as shown by the horizontal strain (Exx, Figures 4c1, 4c2, and 6a). First, right-dipping (i.e., east dipping) normal faults form, associated with a larger horizontal strain closer to the surface. We observed the formation of an "upturning" [*Vidal and Merle*, 2000] accommodating the subsidence of the right part of the ridge (Figure 4, $t = 14$ min), which separates the high horizontal displacement velocity (Figure 4a2) from the low-velocity area, and the low vertical displacement velocity (Figure 4b2) from the high-velocity area. This material above the fault is affected by compression as shown by the horizontal strain (Figure 4c2). To the left of the fault, no deformation, either vertical or horizontal, is observed to affect the sand ridge (Figures 4 and 6a, at $t = 2$ and 14 min).

At $t = 15$ min, the intrusion of the silicone into the sand ridge starts. The effect is instantaneous (Figure 4, $t = 16$ min) and shows an overall major deformation in the half sand ridge. We observe the formation of a graben structure above the intrusion (see also Figure 6a, $t = 14$ to 30 min). The previously undisturbed part of the sand ridge is now largely moving toward the right (Figures 4a3–4a5). The normal fault activity (piston subsidence) induces mainly vertical displacement (Figures 4b3–4b5). The time evolution shows that the two parts are separated by a compressive zone above the basement fault, evidencing an inversion of the stress regime at the normal fault during the intrusion (Figures 4c2 and 4c3). The movement of the flank created by the silicone intrusion produces an evident reverse kinematic on the left-dipping faults of the upturning (see also Figure 6a, $t = 16$ to 30 min). During the transition of nonintrusion/subsiding to intrusion/subsiding

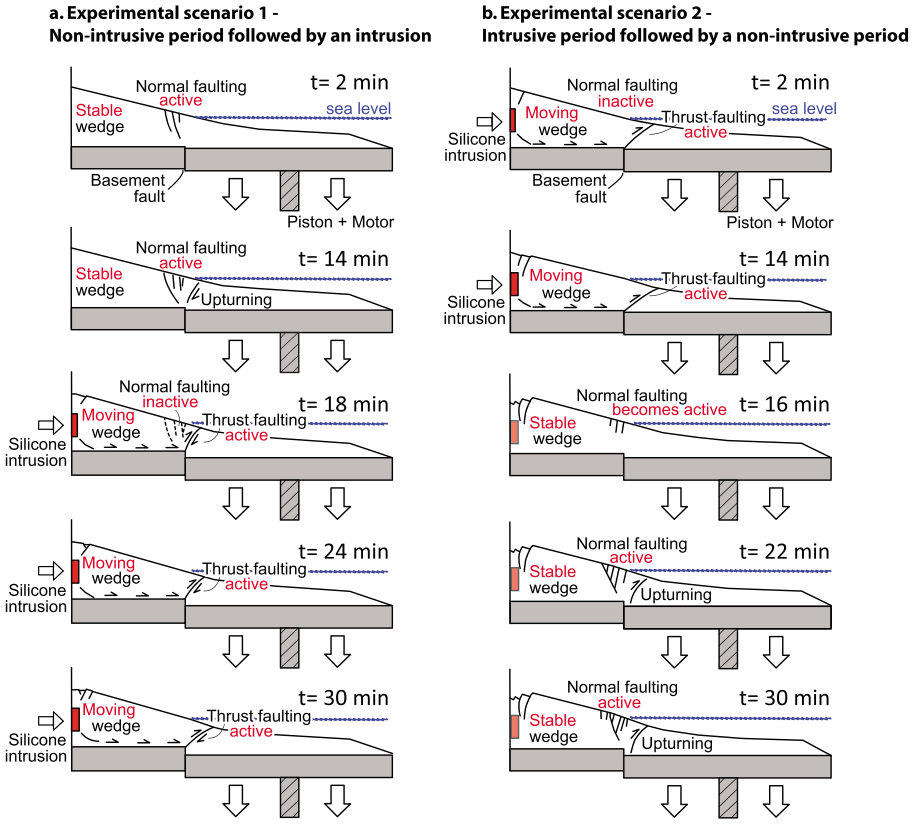


**Figure 6.** Structural summary of the active and inactive faults as seen in the two experimental scenarios. See text for details.

period, the tensile fractures affecting the middle part of the model are clamped as soon as the intrusion starts (Figure 4c3; Exx).

### 4.2. Deformation and Structural Change During and After an Intrusion

The second set of experiments aims to analyze the structural changes associated with the end of an intrusion. In summary, the sand ridge is intruded by silicone during the first half of the experiment (Figures 5 and 6b). The deformation affecting the sand ridge is similar to the previous experiment; the left part of the ridge is pushed by the intrusion and is characterized by high horizontal displacement velocity (Figures 5a1 and 5a2). Only the right part of the ridge is affected by the constant piston subsidence (Figures 5b1 and 5b2). Strain analysis shows that a reverse fault separates the two zones (Figure 5c2). At $t = 15$ min, we stop the intrusion by closing the tank. The first effect observed is the arrest of deformation in the left part of the ridge, while the right part continues to be affected by the piston subsidence. We observe a zone, between the stable part and the subsiding part, which accelerates its motion (Figures 5a3–5a5). This zone is subject to less vertical deformation (Figures 5b3–5b5) than the subsiding part and shows the formation of tensile cracks (Figure 6b).

## 5. Discussion

The detailed analysis of the internal deformation of a deforming volcano flank helps us to understand the interaction among coupled mechanisms, such as tectonic movement, magmatic intrusion, and gravitational deformation. Earlier experimental studies showed that the structural architecture of volcanoes is closely associated to gravitational loading and spreading [*Van Wyk De Vries and Francis*, 1997], tectonic fault activity [*Van Wyk De Vries and Merle*, 1998], and to a combination of gravitational loading and intrusions [*Le Corvec and Walter*, 2009]. Using analogue models, we simulate the interplay between faulting activity and flank motion during magmatic intrusion.

### 5.1. Assumptions and Limitations

The experiments described are based on a number of assumptions. Also, the current knowledge on rock physics and geometric simplifications, as well as the used analyzing methods, provide limitations that need to be discussed. Analogue models simplify nature in order to properly understand specific mechanisms of deformation. In our model, we assume that the west flank of Mount Etna is acting as a buttress, although geophysical and geodetic data suggest that the west flank moves toward the west, but at much lower rate with respect to the east flank [*Bonforte et al*., 2009; *Solaro et al*., 2010]. We further assume that the basic concept that considers the east flank as subject to gravitational spreading and sliding over a décollement surface to be correct. In order to simplify the different models of the décollement surface below Mount Etna [*Borgia et al*., 1992; *Lo Giudice and Rasà*, 1992; *Puglisi et al*., 2008; *Aloisi et al*., 2011], we consider a deep flat décollement surface in our experiments. The results of the two sets of experiments during nonintrusive periods (Figures 4 and 6a, at $t = 2$ and 14 min, and Figures 5 and 6b, at $t = 18$, 24, and 30 min) show no deformation within the sand ridge (e.g., listric fault formation [*Le Corvec and Walter*, 2009]) suggesting that gravitational loading has no influence on the deformation of our model. The deep flat décollement surface being a first-order approximation is not consistent with nature; however, as previous studies show, the décollement configuration might be more complex [*Borgia*, 1994], possibly dipping eastward [*Palano et al*., 2008; *Puglisi et al*., 2008; *Aloisi et al*., 2011] or including more than one décollement [*Tibaldi and Groppelli*, 2002]. The observed deformation during the nonintrusive period of our experiments is principally controlled by tectonic faulting, while the décollement surface enables the flank's lateral movement during intrusive periods accordingly to the similar results of *Le Corvec and Walter* [2009] and *Walter et al*. [2005]. Thus, we neglected the influence of gravitational spreading and focused on the interaction between the magmatic intrusion and the tectonic activity. Finally, when opening or closing the tank trapdoor, the sand ridge has been slightly disturbed. This may cause artifacts in the deformation field, but these remain in the direct vicinity of the trapdoor. In addition, the deformation associated with the opening and closure is short enough in time and does not affect the general deformation of the sand ridge.

The thickness of the dike is only approximated. Overall, the thickness of the simulated dikes is increasing during the experimental run. The dike intrusion rate varies from 3 to $5 \times 10^{-2}$ m $h^{-1}$ (Table 1); we observed that changes within the sand ridge were instantaneous (on the order of seconds to ten of seconds). The intrusion rate of silicone, behaving as a Newtonian fluid [*ten Grotenhuis et al*., 2002], is linear. Therefore, we assume the width of the intrusion after 10 s ranges from ~$10^{-5}$ to ~$10^{-4}$ m, which is the same or an order of magnitude higher than natural dikes [*Rubin*, 1995], taking into account our scaling ratio. In other words, the width of a silicon intrusion in our experiments is more realistic to the size of a single dike in nature during the early moment after opening the trapdoor of the tank. In addition, we observe that most of the deformation in our model occurs soon after the beginning of the silicone intrusion.

Despite these limitations, the kinematics and structural activity of Mount Etna's east flank during the 2001 eruptive sequence can be better understood by comparing our model with GPS data.

### 5.2. Comparison to Mount Etna

Observation of both intrusive and nonintrusive periods at Mount Etna has shown different but characteristic patterns of deformation. Periods of magmatic intrusion are generally characterized by high mobility of the volcanic flank due to the dike emplacement [*Bonforte and Puglisi*, 2003; *Neri et al*., 2004; *Bonforte et al*., 2013a]. These are associated with a significant stress changes at the décollement [*Walter et al*., 2005; *Currenti et al*., 2008], capable of triggering flank displacement. As an example, the 2001 eruption was characterized by a forceful eccentric intrusion [*Bonforte et al*., 2009]. On the other hand, periods of minor magmatic activity are reflective of a more stable flank, affected by seaward gravitational spreading [*Froger et al*., 2001], tectonic deformation at the TFS [*Bonforte and Puglisi*, 2006; *Puglisi et al*., 2008], and faults bounding the volcano east flank [*Neri et al*., 2009; *Solaro et al*., 2010; *Bonforte et al*., 2011].

During the 2001 preeruptive period, GPS data depicted eastward motion mostly restricted to the TFS and uplift in the area near the coastline (Figures 2a1 and 2b1). The possible mechanism has been defined as a set of subvertical faults connected to a basal décollement [*Puglisi et al*., 2008]. The TFS, however, is not a reverse set of faults but consists of east dipping normal faults [*Azzaro*, 1999]. The faulting occurring at the TFS in our models, instead of representing reverse faulting as modeled by *Puglisi et al*. [2008], show subsidence

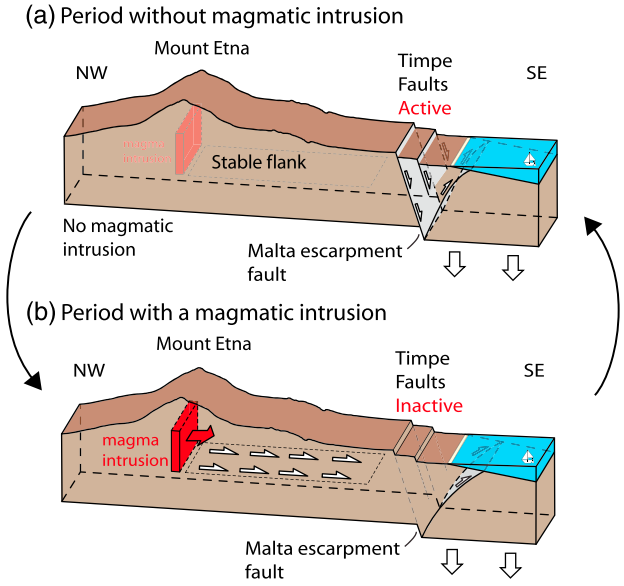


**Figure 7.** Sketch of Mount Etna volcano showing major faults activity (a) during a quiescent period and (b) during a period of rift intrusion.

along normal set of faults (Figures 4 and 6a, at $t = 2$ and 14 min; and Figures 5 and 6b, at $t = 18$ to 30 min). The deformation resulting from our experiment in nonintrusive preeruptive period shows a similar pattern to the GPS data of *Puglisi et al.* [2008] (Figures 2a1 and 2a3). The activity in our model is restricted to the distal part of the experiment affected by the movement along the Malta escarpment. A set of normal faults develops at the volcano surface, connected to the fault scarp (Figures 4 and 6a, at $t = 2$ and 14 min), while no displacement occurs on the flank. The GPS data, however, show that horizontal displacement is also occurring westward of the TFS. This discrepancy between the GPS data and our model could be the result of the difference between the décollement geometry and structural complexities that our simple setup does not account for.

As soon as the intrusion occurs in our models, we observe a change in the sand ridge kinematics. The forceful silicone intrusion is coherently pushing the flank outward. GPS data suggest a significant acceleration of the upper and middle parts of the flank [*Puglisi et al.*, 2008] (Figure 2a2), in good agreement with our models. One important feature shown by the GPS data is the low deformation affecting the TFS and the coastline (Figures 4–6). *Puglisi et al.* [2008] interpret the TFS to be locked due to compression induced by the intrusion, which is again in good accordance with our models (Figures 4 and 6a, at $t = 16$ min).

When the intrusion ends, the deformation of the upper flank also ends, as shown by the GPS data of *Puglisi et al.* [2008] (Figure 2a3). Our experiment (set 2) shows the transition from intrusive period to nonintrusive period and clarifies that once an intrusion stops, the structural activity also changes at the faults related to the TFS (Figure 5, at $t = 18$ to 30 min). While most of the flank becomes stable, the deformation resumed at the TFS and along the coastline [*Puglisi et al.*, 2008] (Figure 2a3). This scenario may be explained by the release of the stress accumulated during the eruption. Again, our experiments are consistent with the general deformation affecting the east flank (Figures 5 and 6b, at $t = 18$ to 30 min). GPS data after the end of the eruption (September to October) measure important uplift east to the TFS and a narrow subsiding zone (Figure 2b3). We consider the strong uplift to be related to delayed release of the compressive strain accumulated during the intrusion period (minor uplift was already visible), while the subsiding zone is in agreement with the analogue model (Figures 5b3–5b5).

Our results focused on the 2001 eruptive episode and its effect on the TFS. It is not yet clear whether the TFS is directly associated to a deep basement fault such as the Malta escarpment [e.g., *Lanzafame and Bousquet*, 1997] or whether the TFS is a near-surface structural expression that has developed in response of a steep slope, possibly close to a tectonic basement fault [*Chiocci et al.*, 2011]. Geodetic data demonstrate that the TFS is involved in the eastward movement of the sliding flank, which appears to be contradicting the hypothesis of a direct connection to a regional tectonic structure [*Bonforte and Puglisi*, 2006]. Whatever the association of the TFS to a deeper basement fault, it remains beyond the scope of this work. Nevertheless, this study argues that any fault system, such as the TFS, may be activated or locked in association with nonintrusive or intrusive periods at Mount Etna.

Finally, this study shows the importance of the strong coupling between magmatism and faulting occurring in an active volcanic system (Figure 7). The interaction between the two systems has a significant role in the activity and stability of the volcano.

## 6. Conclusions

We use analogue experiments to simulate the interaction between tectonic faulting and magmatic intrusion. Our results suggest that during a nonintrusion period, the volcano is affected by slow sliding and displacements limited to the Timpe Fault System, while the rest of the volcano remains stable (Figure 7a). During an intrusion period, most of the volcano flank is affected by large horizontal displacement and the deformation above the TFS is clamped (Figure 7b). Once the intrusion stops, the volcano becomes stable and the activity of the TFS structures restarts. Our results are also in good agreement with geodetic data (GPS) recorded during the 2001 eruption at Mount Etna. Hazards linked to the reactivation of a fault system have therefore more chance to occur during nonintrusive periods, as shown by our experiments.

**Acknowledgments**

We welcome the technical discussions and laboratory support by Matthias Rosenau, Thomas Ziegenhagen, and Onno Oncken. All experiments were done in the GFZ analogue modeling facility. We thank Andrea Borgia, Craig Magee, Gianluca Norini, João Duarte, and Matthieu Kervyn for their thoughtful reviews and constructive comments that significantly improved the manuscript. Financial support by the GFZ Potsdam and the German Research foundation is greatly appreciated. Data supporting this manuscript are available through the main author.

## References

Acocella, V., and M. Neri (2005), Structural features of an active strike-slip fault on the sliding flank of Mt. Etna (Italy), *J. Struct. Geol.*, *27*(2), 343–355.

Adam, J., J. L. Urai, B. Wieneke, O. Oncken, K. Pfeiffer, N. Kukowski, J. Lohrmann, S. Hoth, W. van der Zee, and J. Schmatz (2005), Shear localisation and strain distribution during tectonic faulting—New insights from granular-flow experiments and high-resolution optical image correlation techniques, *J. Struct. Geol.*, *27*(2), 283–301.

Aloisi, M., M. Mattia, C. Monaco, and F. Pulvirenti (2011), Magma, faults, and gravitational loading at Mount Etna: The 2002–2003 eruptive period, *J. Geophys. Res.*, *116*, B05203, doi:10.1029/2010JB007909.

Alparone, S., A. Bonaccorso, A. Bonforte, and G. Currenti (2013), Long-term stress–strain analysis of volcano flank instability: The eastern sector of Etna from 1980 to 2012, *J. Geophys. Res. Solid Earth*, *118*, 5098–5108, doi:10.1002/jgrb.50364.

Argnani, A., F. Mazzarini, C. Bonazzi, M. Bisson, and I. Isola (2013), The deformation offshore of Mount Etna as imaged by multichannel seismic reflection profiles, *J. Volcanol. Geotherm. Res.*, *251*(0), 50–64.

Azzaro, R. (1999), Earthquake surface faulting at Mount Etna volcano (Sicily) and implications for active tectonics, *J. Geodyn.*, *28*(2–3), 193–213.

Azzaro, R., D. Bella, L. Ferreli, A. Maria Michetti, F. Santagati, L. Serva, and E. Vittori (2000), First study of fault trench stratigraphy at Mt. Etna volcano, Southern Italy: Understanding Holocene surface faulting along the Moscarello fault, *J. Geodyn.*, *29*(3–5), 187–210.

Azzaro, R., A. Bonforte, S. Branca, and F. Guglielmino (2013), Geometry and kinematics of the fault systems controlling the unstable flank of Etna volcano (Sicily), *J. Volcanol. Geotherm. Res.*, *251*(0), 5–15.

Barreca, G., A. Bonforte, and M. Neri (2013), A pilot GIS database of active faults of Mt. Etna (Sicily): A tool for integrated hazard evaluation, *J. Volcanol. Geotherm. Res.*, *251*(0), 170–186.

Behncke, B., and M. Neri (2003), The July–August 2001 eruption of Mt. Etna (Sicily), *Bull. Volcanol.*, *65*(7), 461–476.

Bonaccorso, A. (1996), Dynamic inversion of ground deformation data for modelling volcanic sources (Etna 1991–93), *Geophys. Res. Lett.*, *23*(5), 451–454, doi:10.1029/96GL00418.

Bonaccorso, A., and P. M. Davis (1993), Dislocation modelling of the 1989 dike intrusion into the flank of Mount Etna, Sicily, *J. Geophys. Res.*, *98*(B3), 4261–4268, doi:10.1029/92JB02135.

Bonaccorso, A., F. Ferrucci, D. Patanè, and L. Villari (1996), Fast deformation processes and eruptive activity at Mount Etna (Italy), *J. Geophys. Res.*, *101*(B8), 17,467–17,480, doi:10.1029/96JB01151.

Bonaccorso, A., M. Aloisi, and M. Mattia (2002), Dike emplacement forerunning the Etna July 2001 eruption modeled through continuous tilt and GPS data, *Geophys. Res. Lett.*, *29*(13), 1624, doi:10.1029/2001GL014397.

Bonforte, A., and G. Puglisi (2003), Magma uprising and flank dynamics on Mt. Etna volcano, studied by GPS data (1994–1995), *J. Geophys. Res.*, *108*(B3), 2153, doi:10.1029/2002JB001845.

Bonforte, A., and G. Puglisi (2006), Dynamics of the eastern flank of Mt. Etna volcano (Italy) investigated by a dense GPS network, *J. Volcanol. Geotherm. Res.*, *153*(3–4), 357–369.

Bonforte, A., F. Guglielmino, M. Palano, and G. Puglisi (2004), A syn-eruptive ground deformation episode measured by GPS, during the 2001 eruption on the upper southern flank of Mt Etna, *Bull. Volcanol.*, *66*(4), 336–341.

Bonforte, A., A. Bonaccorso, F. Guglielmino, M. Palano, and G. Puglisi (2008), Feeding system and magma storage beneath Mt. Etna as revealed by recent inflation/deflation cycles, *J. Geophys. Res.*, *113*, B05406, doi:10.1029/2007JB005334.

Bonforte, A., S. Gambino, and M. Neri (2009), Intrusion of eccentric dikes: The case of the 2001 eruption and its role in the dynamics of Mt. Etna volcano, *Tectonophysics*, *471*(1–2), 78–86.

Bonforte, A., F. Guglielmino, M. Coltelli, A. Ferretti, and G. Puglisi (2011), Structural assessment of Mount Etna volcano from Permanent Scatterers analysis, *Geochem. Geophys. Geosyst.*, *12*, Q02002, doi:10.1029/2010GC003213.

Bonforte, A., F. Guglielmino, and G. Puglisi (2013a), Interaction between magma intrusion and flank dynamics at Mt. Etna in 2008, imaged by integrated dense GPS and DInSAR data, *Geochem. Geophys. Geosyst.*, *14*, 2818–2835, doi:10.1002/ggge.20190.

Bonforte, A., A. Carnazzo, S. Gambino, F. Guglielmino, F. Obrizzo, and G. Puglisi (2013b), A multidisciplinary study of an active fault crossing urban areas: The Trecastagni Fault at Mt. Etna (Italy), *J. Volcanol. Geotherm. Res.*, *251*(0), 41–49.

Borgia, A. (1994), Dynamic basis of volcanic spreading, *J. Geophys. Res.*, *99*(B9), 17,791–17,804, doi:10.1029/94JB00578.

Borgia, A., L. Ferrari, and G. Pasquare (1992), Importance of gravitational spreading in the tectonic and volcanic evolution of Mount Etna, *Nature*, *357*(6375), 231–235.

Bousquet, J. C., and G. Lanzafame (2001), New interpretation of the flank eruption fractures on Mt. Etna: Consequences for the tectonic framework of the volcano. Nouvelle interprétation des fractures des éruptions latérales de l'Etna: Conséquences pour son cadre tectonique, *Bull. Soc. Geol. Fr.*, *172*(4), 455–467.

Briole, P., R. Gaulon, G. Nunnari, G. Puglisi, and J. C. Ruegg (1992), Measurements of ground movement on Mount Etna, Sicily: A systematic plan to record different temporal and spatial components of ground movement associated with active volcanism, *Volcanic Seismol.*, *3*, 120–129.

Burchardt, S., and T. Walter (2010), Propagation, linkage, and interaction of caldera ring-faults: Comparison between analogue experiments and caldera collapse at Miyakejima, Japan, in 2000, *Bull. Volcanol.*, *72*(3), 297–308.

Chiocci, F. L., M. Coltelli, A. Bosman, and D. Cavallaro (2011), Continental margin large-scale instability controlling the flank sliding of Etna volcano, *Earth Planet. Sci. Lett.*, *305*(1–2), 57–64.
Currenti, G., C. Del Negro, G. Ganci, and D. Scandura (2008), 3D numerical deformation model of the intrusive event forerunning the 2001 Etna eruption, *Phys. Earth Planet. Inter.*, *168*(1–2), 88–96.
Donnadieu, F., and O. Merle (1998), Experiments on the identation process during cryptodome intrusions: New insights into Mount St. Helens deformation, *Geology*, *26*(1), 79–82.
Froger, J. L., O. Merle, and P. Briole (2001), Active spreading and regional extension at Mount Etna imaged by SAR interferometry, *Earth Planet. Sci. Lett.*, *187*(3–4), 245–258.
Houlie, N., P. Briole, A. Bonforte, and G. Puglisi (2006), Large scale ground deformation of Etna observed by GPS between 1994 and 2001, *Geophys. Res. Lett.*, *33*, L02309, doi:10.1029/2005GL024414.
Hubbert, M. K. (1937), Theory of scale models as applied to the study of geologic structures, *Geol. Soc. Am. Bull.*, *48*(10), 1459–1519.
Kieffer, G. (1985), *Evolution structurale et dynamique d'un grand volcan, polygénique: Stades d'édification et activité actuelle de l'Etna (Sicile)*, 497 pp., Annales scientifiques de l'Université de Clermont-Ferrand II, Clermont-Ferrand, France.
Lanzafame, G., and J. C. Bousquet (1997), The Maltese escarpment and its extension from Mt. Etna to the Aeolian Islands (Sicily): Importance and evolution of a lithosphere discontinuity, *Acta Vulcanologica*, *9*(1–2), 113–120.
LaVision (2002), StainMaster Manual for DaVis 6.2. LaVision GmbH, Goettingen.
Le Corvec, N., and T. R. Walter (2009), Volcano spreading and fault interaction influenced by rift zone intrusions: Insights from analogue experiments analyzed with digital image correlation technique, *J. Volcanol. Geotherm. Res.*, *183*(3–4), 170–182.
Lentini, F. (1982), The geology of the Mt. Etna basement, *Mem. Soc. Geol. It*, *23*, 7–25.
Lo Giudice, E., and R. Rasà (1992), Very shallow earthquakes and brittle deformation in active volcanic areas: The Eatnean region as an example, *Tectonophysics*, *202*(2–4), 257–268.
Lundgren, P., F. Casu, M. Manzo, A. Pepe, P. Berardino, E. Sansosti, R. Lanari, and P. Rosen (2004), ERS InSAR observations of Mt. Etna volcano: Magma inflation and radial spreading, paper presented at European Space Agency, (Special Publication) ESA SP.
Marinoni, L. B. (2001), Crustal extension from exposed sheet intrusions: Review and method proposal, *J. Volcanol. Geotherm. Res.*, *107*(1–3), 27–46.
McGuire, B. (1989), Simulating active volcanoes, *Geol. Today*, *5*(3), 93–96.
McGuire, W. J., and A. D. Pullen (1989), Location and orientation of eruptive fissures and feederdykes at Mount Etna; influence of gravitational and regional tectonic stress regimes, *J. Volcanol. Geotherm. Res.*, *38*(3–4), 325–344.
McGuire, W. J., A. D. Pullen, and S. J. Saunders (1990), Recent dyke-induced large-scale block movement at Mount Etna and potential slope failure, *Nature*, *343*(6256), 357–359.
Merle, O., and A. Borgia (1996), Scaled experiments of volcanic spreading, *J. Geophys. Res.*, *101*(6), 13,805–13,817, doi:10.1029/95JB03736.
Monaco, C., and L. Tortorici (2000), Active faulting in the Calabrian arc and eastern Sicily, *J. Geodyn.*, *29*(3–5), 407–424.
Monaco, C., P. Tapponnier, L. Tortorici, and P. Y. Gillot (1997), Late Quaternary slip rates on the Acireale-Piedimonte normal faults and tectonic origin of Mt. Etna (Sicily), *Earth Planet. Sci. Lett.*, *147*(1–4), 125–139.
Neri, M., V. Acocella, and B. Behncke (2004), The role of the Pernicana Fault System in the spreading of Mt. Etna (Italy) during the 2002–2003 eruption, *Bull. Volcanol.*, *66*(5), 417–430.
Neri, M., V. Acocella, B. Behncke, V. Maiolino, A. Ursino, and R. Velardita (2005), Contrasting triggering mechanisms of the 2001 and 2002–2003 eruptions of Mount Etna (Italy), *J. Volcanol. Geotherm. Res.*, *144*(1–4), 235–255.
Neri, M., F. Casu, V. Acocella, G. Solaro, S. Pepe, P. Berardino, E. Sansosti, T. Caltabiano, P. Lundgren, and R. Lanari (2009), Deformation and eruptions at Mt. Etna (Italy): A lesson from 15 years of observations, *Geophys. Res. Lett.*, *36*, L02309, doi:10.1029/2008GL036151.
Norini, G., and V. Acocella (2011), Analogue modeling of flank instability at Mount Etna: Understanding the driving factors, *J. Geophys. Res.*, *116*, B07206, doi:10.1029/2011JB008216.
Palano, M., G. Puglisi, and S. Gresta (2008), Ground deformation patterns at Mt. Etna from 1993 to 2000 from joint use of InSAR and GPS techniques, *J. Volcanol. Geotherm. Res.*, *169*(3–4), 99–120.
Palano, M., S. Gresta, and G. Puglisi (2009), Time-dependent deformation of the eastern flank of Mt. Etna: After-slip or viscoelastic relaxation?, *Tectonophysics*, *473*(3–4), 300–311.
Patane, D., C. Chiarabba, O. Cocina, P. De Gori, M. Moretti, and E. Boschi (2002), Tomographic images and 3D earthquake locations of the seismic swarm preceding the 2001 Mt. Etna eruption: Evidence for a dyke intrusion, *Geophys. Res. Lett.*, *29*(10), 1497, doi:10.1029/2001GL014391.
Patane, D., et al. (2003), Seismological constraints for the dike emplacement of July-August 2001 lateral eruption at Mt. Etna volcano, Italy, *Ann. Geophys.*, *46*(4), 599–608.
Puglisi, G., and A. Bonforte (2004), Dynamics of Mount Etna Volcano inferred from static and kinematic GPS measurements, *J. Geophys. Res.*, *109*, B11404, doi:10.1029/2003JB002878.
Puglisi, G., A. Bonforte, A. Ferretti, F. Guglielmino, M. Palano, and C. Prati (2008), Dynamics of Mount Etna before, during, and after the July-August 2001 eruption inferred from GPS and differential synthetic aperture radar interferometry data, *J. Geophys. Res.*, *113*, B06405, doi:10.1029/2006JB004811.
Ramberg, H. (1981), Deformation structures in theory and experiments, *Symp. Exp. Theory Geol.*, *103*(1), 131, doi:10.1080/11035898109455225.
Rasa, R., R. Azzaro, and O. Leonardi (1996), Aseismic creep on faults and flank instability at Mount Etna volcano, Sicily, in *Volcano Instability on the Earth and Other Planets*, *Geol. Soc. Spec. Publ.*, vol. 110, pp. 179–192, Geological Society, London.
Roche, O., T. H. Druitt, and O. Merle (2000), Experimental study of caldera formation, *J. Geophys. Res.*, *105*(B1), 395–416, doi:10.1029/1999JB900298.
Rubin, A. M. (1995), Propagation of magma-filled cracks, *Annu. Rev. Earth Planet. Sci.*, *23*, 287–336.
Ruch, J., V. Acocella, F. Storti, M. Neri, S. Pepe, G. Solaro, and E. Sansosti (2010), Detachment depth revealed by rollover deformation: An integrated approach at Mount Etna, *Geophys. Res. Lett.*, *37*, L16304, doi:10.1029/2010GL044131.
Ruch, J., S. Pepe, F. Casu, G. Solaro, A. Pepe, V. Acocella, M. Neri, and E. Sansosti (2013), Seismo-tectonic behavior of the Pernicana Fault System (Mt Etna): A gauge for volcano flank instability?, *J. Geophys. Res. Solid Earth*, *118*, 4398–4409, doi:10.1002/jgrb.50281.
Rust, D., and M. Neri (1996), The boundaries of large-scale collapse on the flanks of Mount Etna, Sicily, in *Volcano Instability on the Earth and Other Planets*, *Geol. Soc. Spec. Publ.*, vol. 110, pp. 193–208, Geological Society, London.
Schellart, W. P. (2000), Shear test results for cohesion and friction coefficients for different granular materials: Scaling implications for their usage in analogue modelling, *Tectonophysics*, *324*(1–2), 1–16.
Siebert, L. (1992), Threats from debris avalanches, *Nature*, *356*(6371), 658–659.
Solaro, G., V. Acocella, S. Pepe, J. Ruch, M. Neri, and E. Sansosti (2010), Anatomy of an unstable volcano from InSAR: Multiple processes affecting flank instability at Mt. Etna, 1994–2008, *J. Geophys. Res.*, *115*, B10405, doi:10.1029/2009JB000820.
ten Grotenhuis, S. M., S. Piazolo, T. Pakula, C. W. Passchier, and P. D. Bons (2002), Are polymers suitable rock analogs?, *Tectonophysics*, *350*(1), 35–47.

Tibaldi, A., and G. Groppelli (2002), Volcano-tectonic activity along structures of the unstable NE flank of Mt. Etna (Italy) and their possible origin, *J. Volcanol. Geotherm. Res.*, *115*(3–4), 277–302.

Van Wyk De Vries, B., and O. Merle (1998), Extension induced by volcanic loading in regional strike-slip zones, *Geology*, *26*(11), 983–986.

Van Wyk De Vries, B., and P. W. Francis (1997), Catastrophic collapse at stratovolcanoes induced by gradual volcano spreading, *Nature*, *387*(6631), 387–390.

Vidal, N., and O. Merle (2000), Reactivation of basement faults beneath volcanoes: A new model of flank collapse, *J. Volcanol. Geotherm. Res.*, *99*(1–4), 9–26.

Walter, T. R., and V. R. Troll (2003), Experiments on rift zone evolution in unstable volcanic edifices, *J. Volcanol. Geotherm. Res.*, *127*(1–2), 107–120.

Walter, T. R., V. Acocella, M. Neri, and F. Amelung (2005), Feedback processes between magmatism and E-flank movement at Mt. Etna (Italy) during the 2002–2003 eruption, *J. Geophys. Res.*, *110*, B10205, doi:10.1029/2005JB003688.

White, D. J., W. A. Take, and M. D. Bolton (2003), Soil deformation measurement using particle image velocimetry (PIV) and photogrammetry, *Geotechnique*, *53*(7), 619–631.